文章编号：1001－9014(2017)03－0283－06

DOI:10.11972/j.issn.1001－9014.2017.03.007

Infrared image reconstruction based on compressed sensing and infrared rosette scanning

JIANG Yi-Lin*, TONG Qi, GAO Li-Peng, WANG Hai-Yan, JI Qing-Bo

(College of Information and Communication Engineering, Harbin Engineering University, Harbin 150001, China)

Abstract: Infrared (IR) sub-imaging guidance technique, which combines the single detector and optical scanning device, is a transition from point-source detection technique to imaging guidance technique. Infrared rosette scan sub-imaging system (IRSSIS) is a class of sub-imaging guidance system. The IRSSIS samples part data of the field of view (FOV) according to a specific pattern and obtains a sub-image including the position information of targets. Compressive imaging in the IRSSIS was studied inspired by the single pixel camera. Compressed sensing (CS) will help to reconstruct IR image in the condition of much fewer samples. The key problem of CS applied to the IRSSIS is the measurement matrix construction. While random measurement matrix has been studied intensively, it is hard to implement. A simple deterministic measurement matrix was proposed for the IRSSIS. Furthermore, a fast and effective recovery algorithm, optimized subspace pursuit algorithm (OSP), was proposed. Simulation results show that the proposed measurement matrices can compress and reconstruct IR image prior to the random Gaussian measurement matrices and random Bernoulli measurement matrices. The proposed recovery algorithm also has a better performance.

Key words: compressed sensing (CS), infrared rosette scan sub-imaging system (IRSSIS), deterministic measurement matrices, optimized subspace pursuit algorithm (OSP)

PACS: 42.30.Va

基于压缩感知和红外玫瑰线扫描的红外图像重构

蒋伊琳*, 佟 岐, 郜丽鹏, 王海艳, 汲清波

(哈尔滨工程大学 信息与通信工程学院,黑龙江 哈尔滨 150001)

摘要:红外亚成像制导技术是由点源探测技术到成像制导技术的一种过渡,由单元探测器和光机扫描装置组成.红外玫瑰线扫描亚成像系统是亚成像制导中的一种,红外玫瑰线扫描亚成像系统按照特定的图案采集视场中的部分数据并得到一幅含有目标位置信息的亚图像.受单像素相机的启发,主要研究红外玫瑰线扫描亚成像系统中的压缩成像.压缩感知可以在更少的采样数据条件下重构红外图像,其应用到红外亚成像制导系统中一个关键的问题就是观测矩阵的构造.关于随机观测矩阵的研究已经比较广泛,但随机矩阵很难实现.本文提出了一种简单的适用于红外玫瑰线扫描亚成像系统的确定性观测矩阵.此外还提出了一种快速有效的恢复算法,称为优化子空间追踪算法.仿真结果显示构造的观测矩阵能够压缩和重构红外图像,且重构效果优于随机高斯观测矩阵和随机伯努利观测矩阵,提出的恢复算法也具有较好的表现.

关 键 词:压缩感知(CS);红外玫瑰线扫描亚成像系统(IRSSIS);确定性观测矩阵;优化子空间追踪算法(OSP)

中图分类号:TN911.73　　**文献标识码**:A

Received date: 2016-07-11, **revised date**: 2016-12-16　　**收稿日期**:2016-07-11, **修回日期**:2016-12-16

Foundation items:Supported by National Natural Science Foundation of China (61571146), and Natural Science Foundation of Heilongjiang Province of China (F201407)

Biography:JIANG Yi-Lin (1980-), male, Harbin, China, Ph. D. Research area is image processing, radar countermeasures and electronic interference. E-mail:jiangyilin@hrbeu.edu.cn

* **Corresponding author**:E-mail:jiangyilin@hrbeu.edu.cn

Introduction

Traditional sampling methods follow Nyquist-Shannon theorem, which is applied to most of current data acquisition systems. The data sampled in this way are enough to recover the original signal, but it produces a large amount of redundancy. Meanwhile, it also brings inconvenience to signal transmission, storage and processing. The emergence of CS provides a new way to reduce the number of samples needed to be processed[1-2]. Consequently, CS theory has an extensive influence in various fields[3-7].

IR sub-imaging guidance technology is used to detect, identify and track targets based on the characteristics of IR objects[8]. It replaces the traditional modulation disk and holds a significant position in the field of precision guidance during its appearance. The sub-imaging guidance technology improves the ability of missile to identify true and false targets. It has many notable advantages compared with television guidance and radar guidance in the guidance accuracy and anti-jamming capability. In addition, it works with high sensitivity and good concealment. On the other hand, the IR sub-imaging guidance technology has some drawbacks such as blur-image and low contrast, which increase the difficulties in detecting, identifying and tracking targets. There are still many problems that can be explored to improve the IR sub-imaging guidance technology.

Single pixel camera captures an image with fewer samples than conventional cameras based on CS theory[9]. We studied the potential application of CS technology for the IRSSIS inspired by the single pixel camera. The single detector has the merits of high sensitivity, fast and low-cost compared with the focal plane array (FPA). The IRSSIS samples part information of the FOV with a specific pattern and gets a low-resolution sub-image. We hope to recovery a high-resolution IR image by CS technology, which includes more interested information about targets.

Uzeler *et al.* conducted a study on the image reconstruction for single detector rosette scanning systems based on CS theory[10]. His work proposed the rosette measurement matrix via vectorizing for each rosette scanning pattern matrix, which corresponds to the circular instantaneous field of view (IFOV) region. Numerical simulation experiments show that the reconstructed images from samples collected by the rosette measurement matrix are of sufficient quality. However, the reconstruction performance of IR image depends on the position of targets in the FOV. The reconstruction performance of the target in the center of the FOV is better than that on the edge. This is the defect of the rosette measurement matrix.

In this paper, we focused on the construction of deterministic measurement matrix for the IRSSIS. Inspired by the rosette scanning pattern, a new class of deterministic measurement matrix was designed. In addition, a fast recovery algorithm was proposed for IR image reconstruction. Simulation experiments validated the reconstruction performance of the proposed measurement matrices and recovery algorithm.

1 Theory and methods

In the IRSSIS, the scanning system scans the total field of view (TFOV) with the IFOV along a rosette pattern. The IFOV of the detector is very small and the size of the corresponding detector can be made small. Therefore, the component noise and background noise are greatly reduced, and the signal to noise ratio (SNR) of target is improved. Theoretical analysis and experimental results demonstrated that the rosette scanning is the most suitable mode in all scanning methods.

The scanning system of the IRSSIS adopts the Cassegrain optical system as shown in Fig. 1(a), which includes two titled prisms[11]. When the two tilted prisms rotate around the spin axis at two different frequencies f_1 and f_2 in the opposite direction, the IR detector receives the radiation of the IFOV with a rosette scanning pattern.

The curve equation of the continuous rosette scanning pattern is shown in Eq. (1), where d is the maximum length of rose petal and equals to the radius of the TFOV, $\omega_1 = 2\pi f_1$ and $\omega_2 = 2\pi f_2$ are the scanning angular frequencies, θ_1 and θ_2 are the initial phases:

$$\begin{cases} a(t) = \dfrac{d}{2}(\cos(\omega_1 t + \theta_1) + \cos(\omega_2 t + \theta_2)) \\ b(t) = \dfrac{d}{2}(\sin(\omega_1 t + \theta_1) - \sin(\omega_2 t + \theta_2)) \end{cases} . \quad (1)$$

The number of petals present in the rosette pattern is denoted as $N = N_1 + N_2$, where $N_1 = f_1/f_R$, $N_2 = f_2/f_R$ and f_R is called the scanning frame, which is the greatest common divisor of f_1 and f_2. The rosette scanning pattern can cover the TFOV, but the sampling in the center region is denser than in other regions as shown in Fig. 1(b).

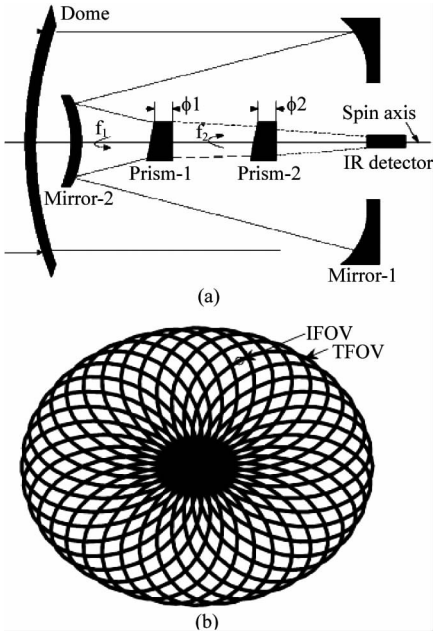

Fig. 1 (a) System architecture, (b) rosette scanning pattern

图1 (a)系统装置,(b)玫瑰线扫描图案

We proposed a deterministic measurement matrix construction via the rosette scanning curve equation. A rosette scanning pattern is performed with $f_1 = 290$ Hz, $f_2 = 70$ Hz, $f_R = 10$ Hz, $d = 128$, $\theta_1 = \theta_2 = 0$. It can be seen that once f_1, f_2 and θ_1, θ_2 are given, a and b of Eq. (1) are only related to t. The time, in which rosette scanning system completes one scan, is $1/f_R = 0.1$ s. We sampled $N_R = 1024$ points during 0.1 s according to Eq. (1) uniformly. $a_n, b_n (n = 0, 1, 2\cdots, 1023)$ were obtained respectively, which can be seen as the instantaneous locations of the IR detector in the TFOV. The proposed deterministic measurement matrix construction is using these instantaneous locations.

Firstly a deterministic sequence $\{\hat{z}_n\}$ can be calculated as follows

$$\begin{cases} z_n = a_n + b_n \\ \hat{z}_n = \sin(z_n) \end{cases} \quad n = 0, 1, 2\cdots, 1023 \quad , \quad (2)$$

then a circulant matrix $\boldsymbol{\Phi}_0 \in R^{N_R \times C}$ (C is a constant) was constructed using the sequence $\{\hat{z}_n\}$ in accordance with the principle of column priority

$$\boldsymbol{\Phi}_0 = \begin{pmatrix} \hat{z}_0 & \hat{z}_0 & \cdots & \hat{z}_0 \\ \hat{z}_1 & \hat{z}_1 & \cdots & \hat{z}_1 \\ \vdots & \vdots & \ddots & \vdots \\ \hat{z}_{N_R-1} & \hat{z}_{N_R-1} & \cdots & \hat{z}_{N_R-1} \end{pmatrix}_{N_R \times C} . \quad (3)$$

If the sampling rate is 0.39, the size of the measurement matrix $\boldsymbol{\Phi}$ should be 100×256. We set the constant $C = 25$ and designed a measurement matrix $\boldsymbol{\Phi} \in R^{100 \times 256}$ by stacking $\boldsymbol{\Phi}_0$, we got

$$\boldsymbol{\Phi} = \begin{pmatrix} \hat{z}_0 & \hat{z}_{100} & \cdots & \hat{z}_{924} \\ \hat{z}_1 & \hat{z}_{101} & \cdots & \hat{z}_{925} \\ \vdots & \vdots & \ddots & \vdots \\ \hat{z}_{99} & \hat{z}_{199} & \cdots & \hat{z}_{N_R-1} \end{pmatrix}_{100 \times 256} . \quad (4)$$

The measurement matrix $\boldsymbol{\Phi} \in R^{100 \times 256}$ was obtained according to the method described above, and measurement matrices of other dimensions can be acquired by truncating the matrix $\boldsymbol{\Phi} \in R^{100 \times 256}$ directly ($30 \leqslant M \leqslant 100$):

$$\boldsymbol{\Phi} = \begin{pmatrix} \hat{z}_0 & \hat{z}_{100} & \cdots & \hat{z}_{924} \\ \hat{z}_1 & \hat{z}_{101} & \cdots & \hat{z}_{925} \\ \vdots & \vdots & \ddots & \vdots \\ \hat{z}_{M-1} & \hat{z}_{M+99} & \cdots & \hat{z}_{M+923} \end{pmatrix}_{M \times 256} . \quad (5)$$

Similarly, we sampled $N_R = 2048$ points uniformly with the same parameters of the rosette scanning system. These points formed a new sequence $\{\hat{z}_n\}$, which can be expressed as follows:

$$\begin{cases} z_n = a_n + b_n \\ \hat{z}_n = \sin(z_n) \end{cases} \quad n = 0, 1, 2\cdots, 2047 \quad , \quad (6)$$

and a new circulant matrix $\boldsymbol{\Phi}_0$ was created using the new sequence:

$$\boldsymbol{\Phi}_0 = \begin{pmatrix} \hat{z}_0 & \hat{z}_0 & \cdots & \hat{z}_0 \\ \hat{z}_1 & \hat{z}_1 & \cdots & \hat{z}_1 \\ \vdots & \vdots & \ddots & \vdots \\ \hat{z}_{N_R-1} & \hat{z}_{N_R-1} & \cdots & \hat{z}_{N_R-1} \end{pmatrix}_{N_R \times 25} . \quad (7)$$

Measurement matrix can be obtained by stacking the circulant matrix $\boldsymbol{\Phi}_0$. The matrix $\boldsymbol{\Phi} \in R^{200 \times 256}$ was constructed by stacking $\boldsymbol{\Phi}_0$, as

$$\boldsymbol{\Phi} = \begin{pmatrix} \hat{z}_0 & \hat{z}_{200} & \cdots & \hat{z}_{1848} \\ \hat{z}_1 & \hat{z}_{201} & \cdots & \hat{z}_{1849} \\ \vdots & \vdots & \ddots & \vdots \\ \hat{z}_{199} & \hat{z}_{399} & \cdots & \hat{z}_{N_R-1} \end{pmatrix}_{200 \times 256} . \quad (8)$$

Similarly, the other dimensional measurement matrices can be designed by truncating the matrix $\boldsymbol{\Phi}$ directly ($100 \leqslant M \leqslant 200$):

$$\boldsymbol{\Phi} = \begin{pmatrix} \hat{z}_0 & \hat{z}_{200} & \cdots & \hat{z}_{1848} \\ \hat{z}_1 & \hat{z}_{201} & \cdots & \hat{z}_{1849} \\ \vdots & \vdots & \ddots & \vdots \\ \hat{z}_{M-1} & \hat{z}_{M+199} & \cdots & \hat{z}_{M+1847} \end{pmatrix}_{M \times 256} . \quad (9)$$

Thus we have constructed a series of different dimensional measurement matrices from the rosette scanning curve.

2 Optimized subspace pursuit

Considering two factors, computational complexity and reconstructed image quality, a new algorithm was proposed for reconstructing IR images, termed OSP algorithm. At present, most of the recovery algorithms are based on the premise that the sparsity of signal is known, but in general it is unknown for the sparsity of an IR image. The subspace pursuit (SP) algorithm designed for sparse signal is a greedy algorithm[12]. For the recovery of IR images, the SP algorithm maybe not work. Hence, we proposed the OSP algorithm based on the SP algorithm to reconstruct IR images. In the SP algorithm, an estimate T^l of size K is maintained and refined during each iteration. These processes were repeated until the residual reaches certain conditions. In the proposed OSP algorithm, an estimate $\hat{\Lambda}_k$ of size $K/5$ is kept and refined during each iteration, and the number of iteration is reduced to 5 without the sparsity of signal known as well. Here, the sparsity level K takes a quarter of the number of measurements. Specific steps are illustrated in Algorithm 1.

Algorithm 1: Optimized Subspace Pursuit Algorithm (OSP)	
Input:	sparsity level K,
	sensing matrix $\boldsymbol{\theta} \in R^{M \times N}$,
	measurements $\boldsymbol{y}$.
Initialization:	iteration number $k = 0$,
	residual vector $\boldsymbol{r}_1 = \boldsymbol{y}$,
	estimated support set $T_0 = \varnothing$.
Iteration:	$k \leftarrow k + 1$,
	$\boldsymbol{p} \leftarrow \boldsymbol{\Theta}^* \boldsymbol{r}_k$,
	$\hat{\Lambda}_k \leftarrow \text{supp}(\boldsymbol{p}_{[K/5]})$,
	$\hat{T}_k \leftarrow T_{k-1} \cup \hat{\Lambda}_k$,
	$\hat{\boldsymbol{x}}_k \leftarrow \boldsymbol{\Theta}_{\hat{T}_k}^{\dagger} \boldsymbol{y}$,
	$T_k \leftarrow supp(\hat{\boldsymbol{x}}_{[K]})$,
	$\boldsymbol{r}_{k+1} \leftarrow \boldsymbol{y} - \boldsymbol{\Theta}_{T_k} \hat{\boldsymbol{x}}_k$.
	Until halting criterion is true.
Output:	The estimated signal $\hat{\boldsymbol{x}} = \boldsymbol{\Psi} \hat{\boldsymbol{x}}_k$

where $\boldsymbol{\Psi}$ is the sparsity dictionary, $\Theta = \boldsymbol{\Phi}\boldsymbol{\Psi}$ denotes the sensing matrix, $\boldsymbol{y} = \boldsymbol{\Phi}\boldsymbol{x}$ represents the measurements.

The procedure of IR compressive imaging based on

CS theory can be described as in Fig. 2.

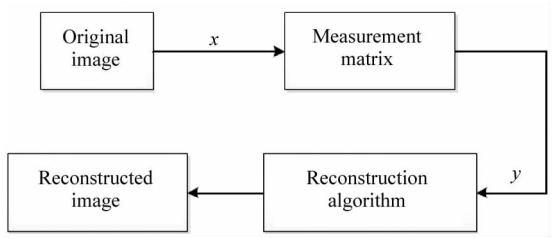

Fig. 2 The flowchart of imaging system based on CS theory
图 2 基于压缩感知理论的成像系统流程图

3 Results and discussion

In this section, we evaluated the performance of the proposed measurement matrices and the OSP algorithm through numerical simulation experiments. We drew a comparison among the proposed deterministic measurement matrices, the random Gaussian matrices and random Bernoulli matrices[13]. The IR image to be reconstructed is of size 256×256. The sparsity dictionary was chosen as the Discrete Cosine Transform (DCT) matrix. The orthogonal matching pursuit (OMP) algorithm was used to reconstruct IR image[14]. The standard of reconstructed IR image was estimated by the peak signal-to-noise ratio (PSNR). PSNR is defined as:

$$PSNR = 20 \cdot \log\left(\frac{255}{\sqrt{(\boldsymbol{x} - \hat{\boldsymbol{x}})^2}}\right) \mathrm{d}B \quad , \quad (10)$$

where $\boldsymbol{x}$ is the original IR image, $\hat{\boldsymbol{x}}$ is the reconstructed IR image, "—" represents the mean.

First we constructed a deterministic measurement matrix by Eq. (4). The reconstructed images using the proposed measurement matrix, the random Gaussian matrix and random Bernoulli matrix are shown in Fig. 3. Figure 3 shows that the proposed measurement matrix outperforms the random Gaussian matrix and random Bernoulli matrix from PSNR values obviously. It can be seen there are much noise in all reconstructed images, and the targets are almost submerged in noise. The reconstruction results can only improve the detection probability. It is worth mentioning that the image reconstructed by the proposed measurement matrix is slightly clear than that by the random Gaussian matrix and random Bernoulli matrix. All reconstructed IR images lose some detail information at lower sampling rate condition.

Figure 4 shows the performance of reconstructed images when the sampling rate is 0.78. We constructed a measurement matrix by Eq. (8), a random Gaussian matrix and a random Bernoulli matrix. In this case, it can be observed that the proposed measurement matrix still outperforms the random Gaussian matrix and random Bernoulli matrix. The PSNR value of reconstructed IR image by the proposed measurement matrix is evidently higher than that by the random Gaussian matrix and random Bernoulli matrix.

Figures 5-6 show the PSNR values of reconstructed IR images under different sampling rates with the proposed deterministic measurement matrices, the random Gaussian matrices and random Bernoulli matrices. It can be observed that the PSNR values of reconstructed images

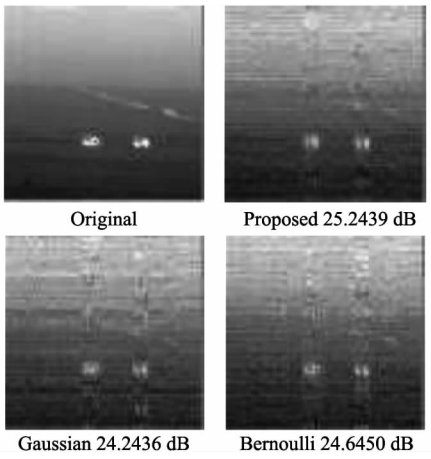

Fig. 3 The PSNR values of reconstructed IR images using random Gaussian matrix, random Bernoulli matrix and the proposed measurement matrix at sampling rate 0.39
图 3 随机高斯矩阵、随机伯努利矩阵和提出的观测矩阵在采样率为 0.39 时的重构红外图像及峰值信噪比值

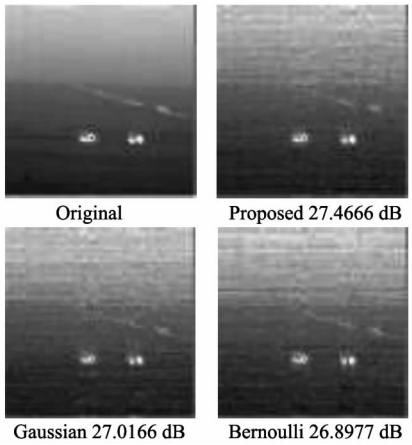

Fig. 4 The PSNR values of reconstructed IR images using random Gaussian matrix, random Bernoulli matrix and the proposed measurement matrix at sampling rate 0.78
图 4 随机高斯矩阵、随机伯努利矩阵和提出的观测矩阵在采样率为 0.78 时的重构红外图像及峰值信噪比值

does not improve as the sampling rate increases, but the general trend is rising. On the whole, the reconstruction performance using the proposed deterministic measurement matrices is markedly better than random Gaussian matrices and random Bernoulli matrices.

We examined the reconstruction performance of OSP algorithm by comparing it with OMP, SP and CoSaMP algorithms[15]. The proposed deterministic matrices are chosen as the measurement matrix. Figures 7-8 show the reconstructed images and corresponding PSNR values with four different recovery algorithms at sampling rate 0.33 and 0.55.

It can be seen that there are notable distinctions in the reconstructed images with different recovery algorithms. In Fig. 7, the PSNR values of reconstructed images by OMP and OSP algorithms are obviously higher than that by SP and CoSaMP algorithms, and the performance of CoSaMP algorithm is the worst among them.

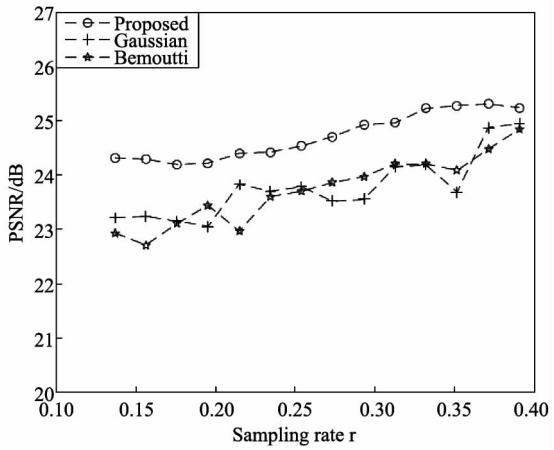

Fig. 5　The relation between sampling rate and PSNR values of reconstructed IR images with the proposed measurement matrices, the random Gaussian matrices and random Bernoulli matrices at sampling rate of 0.13 to 0.39

图 5　提出的观测矩阵与随机高斯矩阵、随机伯努利矩阵在采样率 0.13 到 0.39 之间重构红外图像峰值信噪比关系曲线

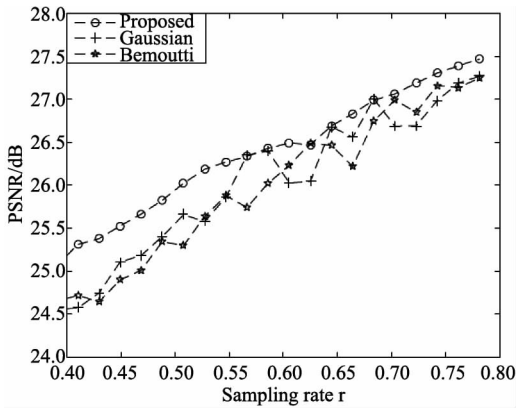

Fig. 6　The relation between sampling rate and PSNR values of reconstructed IR images with the proposed measurement matrices, the random Gaussian matrices and random Bernoulli matrices at sampling rate of 0.39 to 0.78

图 6　提出的观测矩阵与随机高斯矩阵、随机伯努利矩阵在采样率 0.39 到 0.78 之间重构红外图像峰值信噪比关系曲线

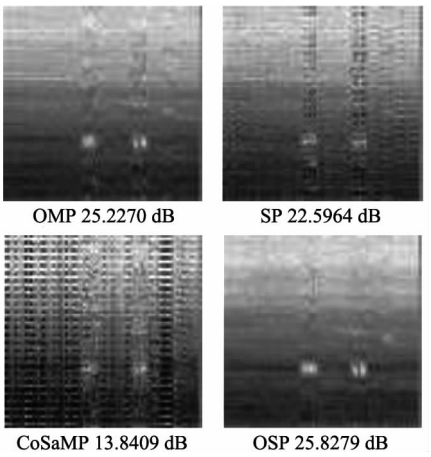

Fig. 7　The reconstruction performance of test image with OMP, SP, CoSaMP and OSP algorithm at sampling rate 0.33

图 7　测试图像在采样率为 0.33 时 OMP、SP、CoSaMP 和 OSP 算法的重构表现

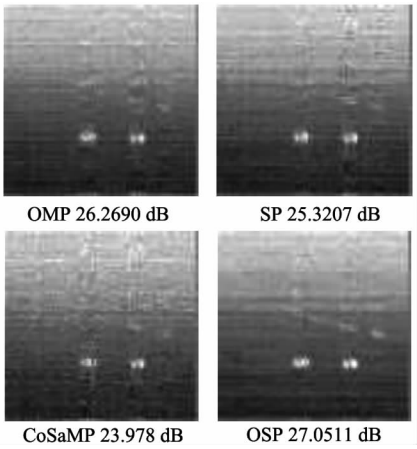

Fig. 8　The reconstruction performance of test image with OMP, SP, CoSaMP and OSP algorithm at sampling rate 0.55

图 8　测试图像在采样率为 0.55 时 OMP、SP、CoSaMP 和 OSP 算法的重构表现

From Fig. 8, it can be observed that the reconstruction performance of SP and CoSaMP algorithms have a greater ascension. However, comparing the four reconstructed images, the PSNR value of reconstructed image by OSP algorithm is also higher than that by OMP, SP and CoSaMP algorithms. The reconstructed image of OSP algorithm is the clearest and more details can be captured by it, which cannot be observed in the remaining three reconstructed images.

4　Conclusions

In this paper, a new deterministic construction of measurement matrices used for the IRSSIS was presented. Besides, a low-complexity recovery algorithm was proposed for the reconstruction of IR image. CS provides a new fashion for the IRSSIS to make the number of samples get reduced greatly and recovery a better quality IR image at the same time. Simulation results demonstrate that the constructed deterministic measurement matrices have a comparable performance with the random Gaussian matrices and random Bernoulli matrices. The OSP algorithm is suitable for IR image reconstruction in accordance with PSNR and visual inspection. The research on the relation between the new deterministic measurement matrices and rosette scanning system will be further studied.

References

[1] Donoho D L. Compressed sensing [J]. *IEEE Transactions on Information Theory*, 2006, **52**(4): 1289 - 1306.

[2] Candes E J, Wakin M B. An Introduction to compressive sampling

[J]. *IEEE Signal Processing Magazine*, 2008, **25**(2):21-30.
[3] Hwang B M, Sang H L, Lim W T, *et al*. A fast spatial-domain terahertz imaging using block-based compressed sensing [J]. *Journal of Infrared, Millimeter, and Terahertz Waves*, 2011, **32**(11):1328-1336.
[4] Yi git E. Compressed sensing for millimeter-wave ground based SAR/ISAR imaging [J]. *Journal of Infrared, Millimeter, and Terahertz Waves*, 2014, **35**(11):932-948.
[5] Herman M A, Strohmer T. High-resolution radar via Compressed sensing [J]. *IEEE Transactions on Signal Processing*, 2009, **57**(6):2275-2284.
[6] Haupt J, Bajwa W U, Raz G, *et al*. Toeplitz compressed sensing matrices with applications to sparse channel estimation [J]. *IEEE Transactions on Information Theory*, 2010, **56**(11):5862-5875.
[7] Abolbashari M, Farahi F. High-resolution hyperspectral single-pixel imaging system based on compressive sensing [J]. *Optical Engineering*, 2012, **51**(7):397-407.
[8] Xiong H, Chen M, Lin Y, *et al*. Analysis of infrared images based on grey system and neural network [J]. *Kybernetes*, 2010, **39**(8):1366-1375.
[9] Duarte M F, Davenport M A, Takbar D, *et al*. Single-pixel imaging via compressive sampling [J]. *IEEE Signal Processing Magazine*, 2008, **25**(2):83-91.
[10] Uzeler H, Cakir S, Aytaç T. Image reconstruction for single detector rosette scanning systems based on compressive sensing theory [J]. *Optical Engineering*, 2016, **55**(2):023108-023108.
[11] Jahng S G, Hong H K, Han S H, *et al*. Dynamic simulation of the rosette scanning infrared seeker and an infrared counter-countermeasure using the moment technique [J]. *Optical Engineering*, 1999, **38**(5):921-928.
[12] Dai W, Milenkovic O. Subspace pursuit for compressive sensing signal reconstruction [J]. *IEEE Transactions on Information Theory*, 2009, **55**(5):2230-2249.
[13] Lu W, Li W, Kpalma K, *et al*. Compressed sensing performance of random bernoulli matrices with high compression ratio [J]. *IEEE Signal Processing Letters*, 2015, **22**(8):1074-1078.
[14] Tropp J A, Gilbert A C. Signal recovery from random measurements via orthogonal matching pursuit [J]. *IEEE Transactions on Information Theory*, 2007, **53**(12):4655-4666.
[15] Needell D, Tropp J A. CoSaMP: iterative signal recovery from incomplete and inaccurate samples[J]. *Applied & Computational Harmonic Analysis*, 2008, **26**(3):301-321.

(上接第282页)

simple microstructure. The laser devices with exceeding 1 W output power were realized. It was found that the deep microstructure could reduce the lateral-mode number more effectively. About 57% and 8% improvement in lateral FF angle were achieved with decreased peak-number and increased power from deeply etched microstructure compared with the devices without and with shallow microstructure. We believe that these results will contribute to the development of high-power low-divergence GaSb based BA diode lasers.

References

[1] Gaimard Q, Triki M, Nguyen-Ba T, *et al*. Distributed feedback GaSb based laser diodes with buried grating: a new field of single frequency sources from 2 to 3 μm for gas sensing applications [J]. *Opt. Express*, 2015, **23**: 19118-19128.
[2] Geerlings E, Rattunde M, Schmitz J, *et al*. Widely tunable GaSb-based external cavity diode laser emitting around 2.3μm [J]. *IEEE Photon. Technol. Lett.*, 2006, **18**: 1913-1915.
[3] Karsten S, Samir L, Philpp K, *et al*. 2μm laser sources and their possible applications [C/OL]. *Frontiers in Guided Wave Optics and Optoelectronics* (*Germany*: *LISA laser products OHG*). 2010(2010-02-1). http://www.intechopen.com.
[4] Belenky G, Shterengas L, Kim J G, *et al*. GaSb-based lasers for spectral region 2-4μm: challenges and limitations [J]. *Proc. SPIE*, 2005, **5732**:169-174.
[5] Rouillard Y, Genty F, Perona A, *et al*. Edge and vertical surface emitting lasers around 2.0~2.5μm and their applications[J]. *Philos. Trans. A*, 2001, **359**: 581-597.
[6] Compeán-Jasso V H, Anda-Salazar F, de Sánchez-Niño F, *et al*. High and abrupt breakdown voltage $In_{0.15}Ga_{0.85}As_{0.14}Sb_{0.86}$/GaSb junctions grown by LPE[J]. *Infrared Phys. Technol.*, 2016, **79**:32-35.
[7] Muller M, Rattunde M, Kaufel G. *et al*. Short-pulse high-power operation of GaSb-based diode lasers[J]. *IEEE Photon. Technol. Lett.*, 2009, **21**: 1770-1772.
[8] Gassenq A. Taliercio, T. Cerutti L, *et al*. Mid-IR lasing from highly tensile-strained, type II, GaInAs/GaSb quantum wells[J]. *Electron. Lett.*, 2009, **45**:1320-1321.
[9] Rattunde M, Schmitz J, Kaufel G, *et al*. GaSb-based 2.X μm quantum-well diode lasers with low beam divergence and high output power [J]. *Appl. Phys. Lett.*, 2006, **88**: 08115.
[10] Wolff S, Rodionov A, Sherstobitov V E, *et al*. Fourier-optical transverse mode selection in external-cavity broad-area lasers: experimental and numerical results [J]. *IEEE Journal of Quantum Electronics*, 2003, **39**(3): 448-458.
[11] Lichtner M, Tronciu V Z, Vladimirov A G, Theoretical investigation of striped and non-striped broad area lasers with off-axis feedback[J]. *IEEE J. Quantum Electron.*, 2012, **48**: 353-360.
[12] Swint R B, Yeoh T S, Elarde V C, *et al*. Curved waveguides for spatial mode filters in semiconductor lasers [J]. *Photon. Technol. Lett.*, 2004, **16**: 12-14.
[13] Wenzel H, Crump P, Fricke J, *et al*. Suppression of higher-order lateral modes in broad-area diode lasers by resonant anti-guiding [J]. *IEEE J. Quantum Electron*, 2013, **49**:1102-1108.
[14] Wenzel H, Bugge E, Dallmer M, *et al*. Fundamental-lateral mode stabilized high-power ridge-waveguide lasers with a low beam divergence [J]. *IEEE Photon. Technol. Lett.*, 2008, **20**: 214-216.
[15] Choi H K, Walpole J N, Turner G W, *et al*. GaInAsSb-AlGaAsSb tapered lasers emitting at 2.05 μm with 0.6 W diffraction-limited power [J]. *IEEE Photon. Technol. Lett.*, 1998, **10**(7): 938-940.
[16] Forouhar S, Briggs R M, Frez C, *et al*. High-power laterally coupled distributed-feedback GaSb-based diode lasers at 2μm wavelength [J]. *Appl. Phys. Lett.*, 2012, **100**: 031107.
[17] Rong J, Xing E, Zhang Y, *et al*. Low lateral divergence 2 μm InGaSb/ AlGaAsSb broad-area quantum well lasers [J]. *Optics Express*, 2016, **24**(7):7246.
[18] Kelemen M T, Weber J, Mikulla M, *et al*. High-power high-brightness tapered diode lasers and amplifiers [J]. *Proc. SPIE*, 2005, **5723**:198-208.
[19] Hecht J. Bringing high brightness to high-power laser diodes [J]. Laser Focus World, 2011, **47**(11): 43-46.
[20] Crump P, Leisher P, Matson T, *et al*. Control of optical mode distribution through etched microstructures for improved broad area laser performance [J]. *Appl. Phys. Lett.*, 2008, **92**: 131113.
[21] Jonathan A F, Mikhail A B. Federico C. Wide-ridge metal-metal terahertz quantum cascade lasers with high-order lateral mode suppression [J]. *Appl. Phys. Lett.*, 2008, **92**: 031106.
[22] Wang L, Tong C. Tian S, *et al*. High-Power Ultralow Divergence Edge-Emitting Diode Laser With Circular Beam [J]. *IEEE J. Sel. Top. Quantum Electron.* 2015, **21**(6):1501609.
[23] Crump P, Pietrzak A, Bugge F, *et al*. 975 nm high power diode lasers with high efficiency and narrow vertical far field enabled by low index quantum barriers[J]. *Appl. Phys. Lett.*, 2010, **96**(13): 131110.